

Plasmonic Light Trapping in Titania–Silver Dots Thin Films

Daniela Manno, Alessandro Buccolieri, Giorgio Giuseppe Carbone, Lucio Calcagnile, and Antonio Serra*

Metal nanoparticles (NPs) in a transparent dielectric matrix represent a very intriguing system due to the plasmonic absorption tunable in the range of visible wavelengths. Herein, the preparation and physical characterization of plasmonic titania–silver dots thin films are reported. The synthesis parameter that leads to making a TiO₂ matrix in which the Ag NPs are actually incorporated is carefully analyzed and controlled. Morphological (scanning electron microscopy, transmission electron microscopy, high resolution electron microscopy), structural (selected area diffraction, X-ray diffraction), and spectroscopic (Raman spectroscopy) characterization techniques attest that the Ag NPs are spherical and homogeneously distributed into the TiO₂ dielectric matrix in the structural modification of anatase. The study of the optical properties of films concludes the work. Plasmonic resonance is analyzed according to the light scattering theory.

1. Introduction

Localized plasmon resonance (LSPR) represents the most intriguing optical property of noble metal nanoparticles (NPs). The development of synthesis methods to obtain NPs of different materials of various shapes and sizes has allowed to advance and understand the applications of LSPR spectroscopy.^[1,2]

Due to this function, nanostructured materials have the potential to play a very important role in various application fields,^[3] such as colorimetric sensors,^[4] data storage,^[5] and biomedical diagnostic applications.^[6] Because shape and position of LSPR peak depend not only on NPs material, size, and shape but also on surrounding medium,^[7] various nanostructures have been synthesized and used to modulate LSPR among these NPs,^[8] nanorods,^[9] nanoporous films,^[10] and nanohole arrays.^[11]

Nowadays, plasmonic metamaterials (metal–dielectric compounds) with peculiar optical properties such as the modulation of plasmonic resonance, constitute a very intriguing research

field for their applications.^[12,13] The possibility of designing and manufacturing linear metamaterials has allowed the realization of efficient devices for holography with the potential to incorporate information can also be incorporated into the width of each nanometric element, therefore, as the resolution is not limited by optical diffraction, achieves higher data density than standard films.^[14]

Metal NPs in a transparent dielectric matrix establish a typical nanocomposite material characterized by plasmonic absorption in the range of visible wavelengths.^[15] In addition, plasmon resonance can mediate processes such as photoexcitation of carriers and give rise to potential applications in photocatalysis,^[16–18] photovoltaics,^[19,20] photoanode-based dye-sensitized solar


cells,^[21–23] and photocatalysis degradation.^[24,25] Plasmonic nanostructures have another peculiar property that makes them potentially attractive in the realization of optical and optoelectronic systems such as lenses, solar cells, and photodetectors. Baryshnikova et al. showed that silver and silicon NP arrays can be used as antireflective coatings in the visible spectral range.^[26]

For example, Nakayama et al. demonstrated that it is possible to obtain an improvement in the efficiency of GaAs solar cells by decorating the surface with appropriately sized Ag NPs.^[27] Gold NPs, acting as back-reflector, can increase the energy conversion efficiency in hydrogenated amorphous silicon due to the widespread diffusion of light through the effects of resonant plasmon excitation.^[28] Some theoretical studies have hypothesized that optical devices with negative refraction have the possibility of increasing the refractive power of a lens.^[29] Luo et al.^[30] reported about stratified plasmonic nanostructures dispersed in a dielectric matrix that have the above feature and can realize microscopy beyond the diffraction limit.

Plasmon resonance is also a useful trick to allow high-gap semiconductors to respond in the visible region of the electromagnetic spectrum. For example, TiO₂, known for photocatalytic applications, has the disadvantage of having the energy gap in the ultraviolet (UV) region (respectively, 3.2 and 3.0 eV for anatase and rutile^[31]). To improve and overcome the performance of TiO₂, conventional metallic NPs have been inserted in the dielectric matrix of nanostructured TiO₂ thin films thus obtaining a metamaterial that can be used in different fields. In addition, the sol–gel method represents one of the most widely used methods for synthesizing nanostructured materials, both pure and composite with good chemical homogeneity, due

Prof. D. Manno, Prof. A. Buccolieri, Dr. G. G. Carbone, Prof. L. Calcagnile, Prof. A. Serra

Dipartimento di Matematica e Fisica “Ennio De Giorgi”
INFN – National Institute for Nuclear Physics
CEDAD – Centro di Fisica applicata, Datazione e Diagnostica
Università del Salento
Lecce 73100, Italy
E-mail: antonio.serra@unisalento.it

 The ORCID identification number(s) for the author(s) of this article can be found under <https://doi.org/10.1002/pssb.202000124>.

DOI: 10.1002/pssb.202000124

to its simplicity, low reaction temperature, low requirements for substrates, and high product purity.^[32] This method allowed to obtain modified TiO₂ having an interesting tunable photochromatic behavior, as Cu–TiO₂ hybrid NPs,^[33] or silver-doped titania NPs.^[34]

The strategy of this work is to include plasmonic silver NPs in a titania matrix to obtain optically transparent films with improved optical properties. The silver nanospheres in the titania matrix promote collective resonances that lead to an efficient coupling of light trapping.

In this article, both the preparation of the films and their morphological and structural and optical characterization will be discussed in detail. Particular attention is required for the control of the synthesis parameters that lead to the realization of a TiO₂ matrix in which the Ag NPs are effectively incorporated. Morphological characterization methods (scanning electron microscopy [SEM], transmission electron microscopy [TEM], high-resolution transmission electron microscopy [HREM]), structural (selected area electron diffraction [SAD], X-ray diffraction [XRD]), and spectroscopic (Raman spectroscopy) attest that the Ag NPs are spherical and homogeneously distributed in the TiO₂ dielectric matrix in the structural modification of the anatase. The optical properties and the presence of the plasmon resonance have been carefully analyzed according to the light scattering theory.

2. Experimental Section

2.1. Materials

2-Propanol ($\geq 99.5\%$), Tween 60 (LD50 Rat $> 38\,000\text{ mg kg}^{-1}$), glacial acetic acid ($\geq 99\%$), titanium (IV)-isopropoxide (TTIP, 99.9%), and silver nitrate (AgNO₃, 99%) was all purchased from Sigma Aldrich Corporation (Saint Louis, USA). Silica substrates (Suprasil 100 – Heraeus) were washed by ultrasonication in ethanol for 3 min and then dried with a nitrogen spray gun prior to use.

2.2. Thin-Film Deposition

In a typical synthesis, 12.5 g of Tween and 21.8 mL of 2-propanol were mixed and maintained at room temperature under vigorous stirring until the obtained solution becomes transparent (Mix-A). Different solutions of silver nitrate were prepared by adding 0.10, 0.15, 0.20, and 0.25 g of AgNO₃ to 10 mL of 2-propanol (Mix-B). Then, 3 mL of glacial acetic acid, 2.7 mL of TTIP, and Mix-B were added sequentially to Mix-A with a 30 s gap between them. The final solution (Mix-C) had a pale-yellow color and was maintained at room temperature under vigorous stirring for 15 min.

However, as reported in the Supporting Information, the solution (Mix-B) obtained with 0.1 g of AgNO₃ did not allow to obtain a concentration of silver NPs sufficient for a good plasmonic resonance signal. On the contrary, by increasing the silver concentration (Mix-B with 0.2 and 0.25 g of AgNO₃), a segregation of Ag was observed already in the solution, which gave rise to agglomerates clearly visible toward the outside of the films.

Mix-C was deposited on $2 \times 2\text{ cm}^2$ -sized silica substrates using a spinner device. A spinning speed of 2500 rpm for 1 min allowed to obtain homogeneous coating. As reported in

Supporting Information, lower spinning speed (1500 and 2000 rpm) did not allow an optimal dispersion of the solution on the substrate. A higher speed (3000 rpm) gave rise to a too thin and discontinuous film (with average thickness $< 25\text{ nm}$).

The films after drying at 100 °C for 5 min were subsequently calcined in a programmable multisegment oven (tube-shaped CTF Carbolite tube furnace) at a ramp speed of 5 °C min^{-1} up to 400 °C, maintained at this temperature for 15 min and cooled in 24 h.

The mechanism underlying the formation of TiO₂ NPs was assumed to be attributable to a proton-assisted SN₁ reaction. The H₃O⁺ ion that is released from the acetic acid in solution, induced isopropoxide titanium (Ti-OiPr) to break down into [Ti-(OiPr)₃]⁺ and [OiPr]⁻. Then, the nucleophilic attack of propanol on [Ti-(OiPr)₃]⁺ resulted in the release of propyl cations. Subsequently, all OiPr groups were exchanged with OH, leading to the formation of Ti(OH)₄. The final condensation phase occurred after spinning the solution on the supports and subsequent firing at 100 °C. The dehydration of the samples led to TiO₂ formation.^[35]

However, the formation of the TiO₂ matrix and silver NPs occurred after the calcination process. When titanium dioxide was heated to 400 °C, electron-hole pairs were formed by transferring electrons to the conduction band from the valence band.^[2,3,36,37] Silver ions, which were initially adsorbed on the surface of the TiO₂ particles, were reduced by those electrons, forming silver NPs, according to the mechanism of the formation of TiO₂-silver dots thin film shown in **Figure 1**.

2.3. Characterization

Films thickness measured with a surface profilometer Tencor Alpha Step were in the range 100–200 nm. Electrical measurements were carried out, by a four-point probe Biorad HL5500 Hall effect system in the 200–500 K temperature range at a pressure of 0.1 Pa. Contacting the samples by sputtering gold dots 1 mm in diameter onto films surface in the van der Pauw geometry allowed resistivity and Hall measurements with a magnetic flux of 0.5 T. The lower measurement limit of the Hall mobility was about $0.1\text{ cm}^2\text{ V}^{-1}\text{ s}^{-1}$.

UV–vis spectra were recorded in the range between 250 and 800 nm using a Varian Cary-5 double-beam spectrophotometer equipped by an integrating sphere for reflectance measurements.

Accurate morphological analysis of the surface and nanoscale roughness of our films were obtained by atomic force microscopy (AFM) measurements carried out using a Jeol 4210 STM-AFM microscope. To record all AFM images, we used silicon carbide tips having a radius of curvature smaller than 10 nm and cantilevers with 0.15 N m^{-1} force constant. All observations were carried out in air at room temperature. The average roughness was provided directly by the instrument.

The morphology and elemental composition of the obtained films were carried out using a scanning electron microscope SEM-JEOL JSM 5010LV equipped with an Oxford X-ray energy dispersive (EDX) microanalysis system. All observations were carried out at 20 kV acceleration voltage with an incoming beam having current of 70 μA .

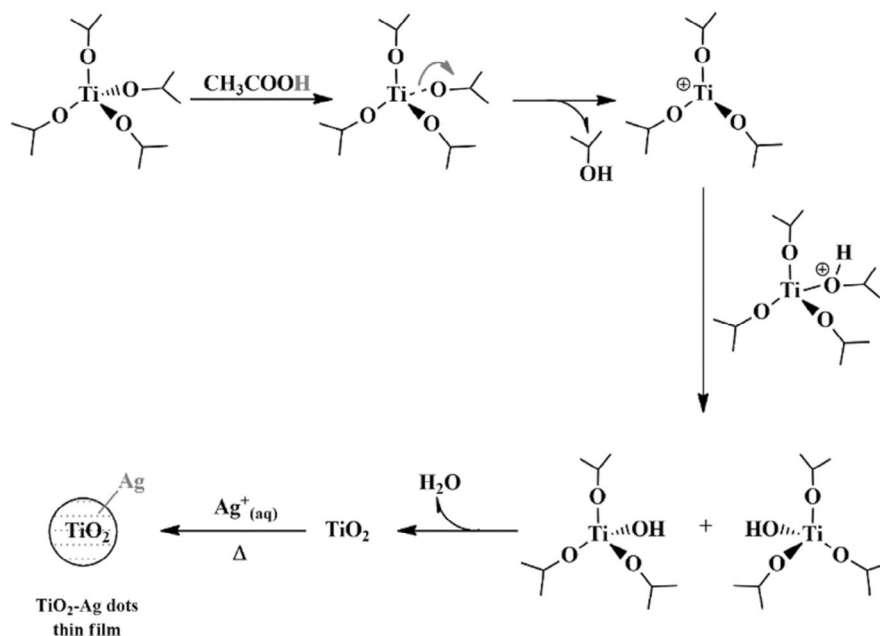


Figure 1. Mechanism of formation of TiO₂-silver dots thin film.

CASINO simulation software^[38] was used to describe the electron trajectories through elastic and inelastic scattering events and to simulate SEM images.

XRD measurements were carried out in the Bragg-Brentano geometry on a Mini Flex Rigaku diffractometer operated at 30 kV voltage and a current of 120 mA with Cu K α radiation ($\lambda = 0.154056$ nm).

Conventional TEM, HREM, and SAD patterns were conducted using a HITACHI 7700 transmission electron microscope operating at 120 kV. The diffraction patterns were recorded by selecting a suitable spot size, convergence angle, and condenser aperture to get the diffraction patterns from chosen areas of about 1000 nm in diameter with an approximately parallel beam (the convergence angle of the incoming beam was about 5×10^{-5} rad). The diffraction patterns were processed by PASAD tools software.^[39] To carry out the TEM observations, films were chemically removed from substrates and deposited onto standard carbon supported 600-mesh copper grid. Raman spectra were acquired by means of a Renishaw Invia Spectrometer equipped by a Leica microscope, the anelastic scattering was promoted by Ar⁺ ions laser irradiation at 514 nm and 25 mW power.

3. Results and Discussion

3.1. Structural and Morphological Analyses

Figure 2a shows a typical EDX spectrum recorded from our films. It is evident the presence of O, Si, Ti, and Ag.

The silicon comes from the silica substrate being the film not thick enough to attenuate all the incoming electrons energy. The films turned out to be made of 8 wt% Ag/TiO₂. **Figure 2b** shows a typical SAD pattern obtained from our film to analyze the structural order.

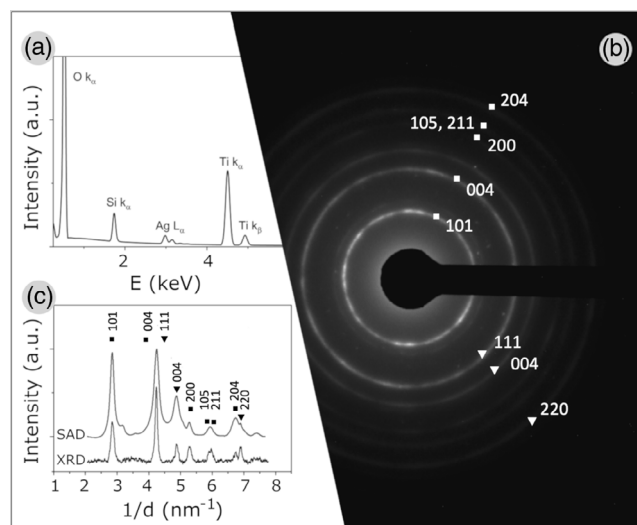


Figure 2. a) EDX elemental analysis of a typical titania-silver dots thin film. b) SAD pattern. c) PASAD-processed SAD compared with XRD pattern. In the figure, the squares refer to the reflections originating from the TiO₂ anatase, whereas the triangles refer to the reflections coming from the silver NPs.

The peculiar features of SAD patterns are continuous rings that indicate a random arrangement of nanocrystals. The geometry of the diffraction rings is not the expected one neither for titanium oxide nor for silver. Then the diffraction pattern has been processed by PASAD tools software, and the diffraction profile obtained by azimuthal integration has been compared with XRD, as shown in **Figure 2c**. To make the comparison more immediate, the XRD diffraction has been plotted as normalized intensity versus $1/d$ as well as the SAD profile. The peaks can be indexed as shown in **Table 1**.

Table 1. Resume of diffraction data interpretation obtained by structural characterization. $1/d$ reports the experimental values of reciprocal lattice spacings deduced by electron and XRDs. “TiO₂ anatase hkl ” shows the corresponding lattice plains of TiO₂ anatase, and, similarly, “Ag hkl ” shows the corresponding lattice plains of face-centered cubic (fcc) silver crystal. “Intensity anatase” and “intensity Ag” are the expected diffraction maxima intensities. For interpretation, see text.

$1/d \text{ nm}^{-1}$	TiO ₂ anatase hkl	Intensity anatase	Ag hkl	Intensity Ag
2.85	101	100	–	–
4.24	004	20	111	100
4.90	–	–	004	47
5.29	200	28	–	–
5.88	105	18	–	–
5.99	211	18	–	–
6.76	204	14	–	–
6.94	–	–	220	25

As shown in Table 1, many of the observed peaks agree to TiO₂ in the anatase structural modification.^[40]

Two peaks at 4.90 and 6.94 nm⁻¹ are compatible with silver reflections (004) and (220), respectively. Only the peak at 4.24 nm⁻¹, the most intense, can be assigned to both reflections (004) of TiO₂ and (111) of Ag. Because the most intense reflection of TiO₂ anatase is the (101) one, the peak at 4.24 nm⁻¹ must undoubtedly be attributed to the reflection (111) of the silver for which the maximum intensity is expected. In conclusion, the obtained films are made by a nanostructured TiO₂ matrix in the anatase structural modification in which silver nanocrystals are dispersed.

Figure 3a shows a typical overview of the film obtained in bright field mode. The typical Z-contrast makes it possible to discriminate between silver grains. As estimated by the XRD, the TEM image confirms that the silver grains are much larger than those of TiO₂ that make up the film matrix. The dispersion of the size of the silver grains (diameter d in nm) is shown in the histogram (inset of Figure 3a).

Further confirmation of the morphology and structure of the film come from high-resolution microscopy. Figure 3b shows a detail of the film at high magnification: two grains are clearly visible. The grains are characterized by clearly different dimensions and contrasts. Two areas were selected onto the two grains and observed in high resolution. As evident from the insets labeled in Figure 3b, the two different grains give rise to two sets of lattice fringes: the larger grain shows the fringes (111) of silver and the smaller grain the fringes (101) of TiO₂.

AFM analysis shows that the analyzed films have an average roughness of 3.4 nm. A typical AFM image, recorded by our films, is shown in Figure 4a and shows that the surface of the film is made up of very flat islands without texturing. However, AFM images did not allow us to resolve the fine structure of each island and the chemical composition of different regions on those images. Fine information on the particle size of the films was obtained from TEM observations.

Unfortunately, neither XRD nor transmission microscopy can provide information on the position of silver grains. In fact, these can be positioned onto the surface, or immersed into

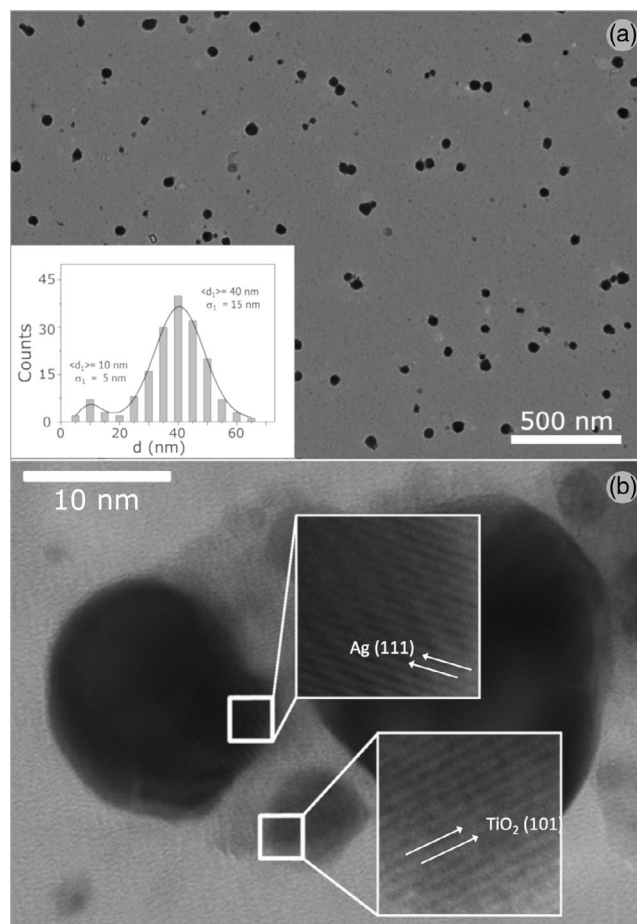


Figure 3. a) Typical overview of titania–silver dots thin film obtained in bright-field mode, the histogram (inset) shows the silver NPs’ size dispersion. b) Enlargement and HREM details of Ag NPs in the TiO₂ matrix.

TiO₂ matrix. Therefore, we carried out SEM observations and used the CASINO software to simulate the generation of backscattered electrons from a set of points over an area of 50 × 50 nm². The model sample consists of a TiO₂ plate of 100 nm thick containing Ag spheres of 40 nm in diameter at different depths from the surface (Figure S2 and S3, Supporting Information, for details).

Figure 4b shows a typical backscattered SEM image. Many bright islands of about 40 nm in diameter are evident on a very regular surface. Three of these islands labeled A, B, and C are shown enlarged in the inset and compared with three related simulations: A’ (the center of the silver sphere is at 20 nm from the surface), B’ (the center of the silver sphere is at 30 nm from the surface), and C’ (the center of the silver sphere is 40 nm from the surface). The agreement is very good and allows us to conclude that, as evidenced by the TEM and SEM results, no NP-AG clusters are created. The silver NPs are randomly dispersed in the TiO₂ matrix and govern the optical properties of the films.

3.2. Electrical Measurements

Hall effect measurements evidence an n-type behavior for all examined films. Figure 5a shows the typical resistivity of a

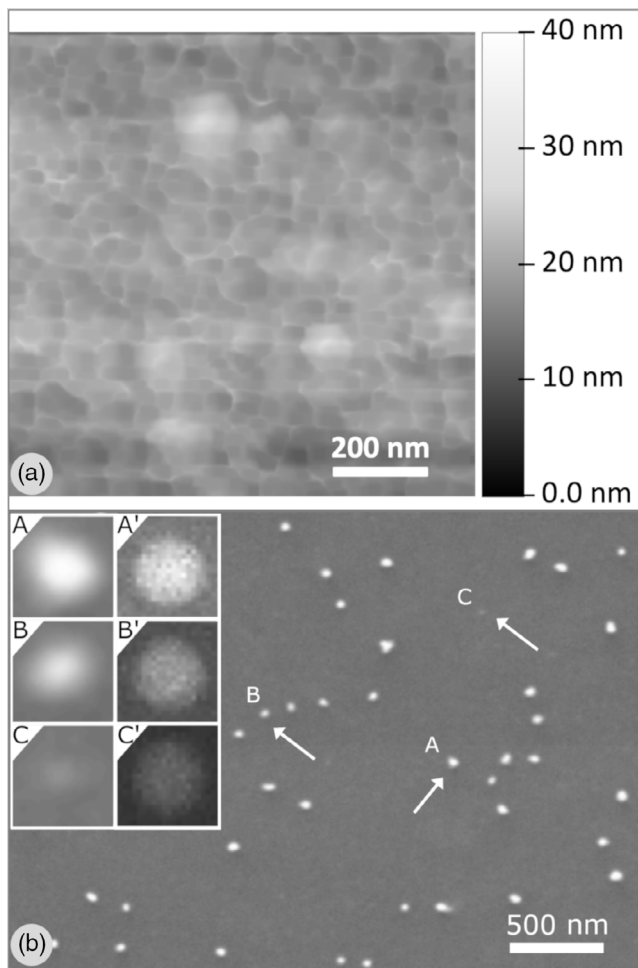


Figure 4. a) AFM image and b) typical backscattered SEM image, recorded from the analyzed film. b) Islands labeled A, B, and C (inset) are compared with backscattered simulated contrast A', B', and C' (inset).

TiO₂-Ag dots film dependence with $1/kT$. The linear behavior confirms that the conduction mechanism is thermally activated, and the line slope allows to determine a conductivity activation energy of about (26 ± 2) meV.

In the investigated temperatures range, the Hall mobility (Figure 5b) of TiO₂-Ag dots films decreases as the temperature increases, such thermally activated mobility [$\mu \propto T^{-1/2} e^{-\frac{\varphi_B}{kT}}$] can be explained by the Petritz model,^[41] which describes thermionic emission of electrons across grain boundaries. Here, φ_B is the energetic height of the intergrain barrier. The linear behavior of experimental data indicates a good agreement over the investigated temperature range, and a mobility activation energy of (28 ± 2) meV can be determined, which provides a good match with the conductivity activation energy. This dependence indicates that the electrical properties of TiO₂-Ag dot films obtained here are dominated by the grain boundary scattering.

Figure 5c shows the carrier concentrations in the investigated temperature range, as evident, the carrier concentration is almost temperature independent. That means, these films show

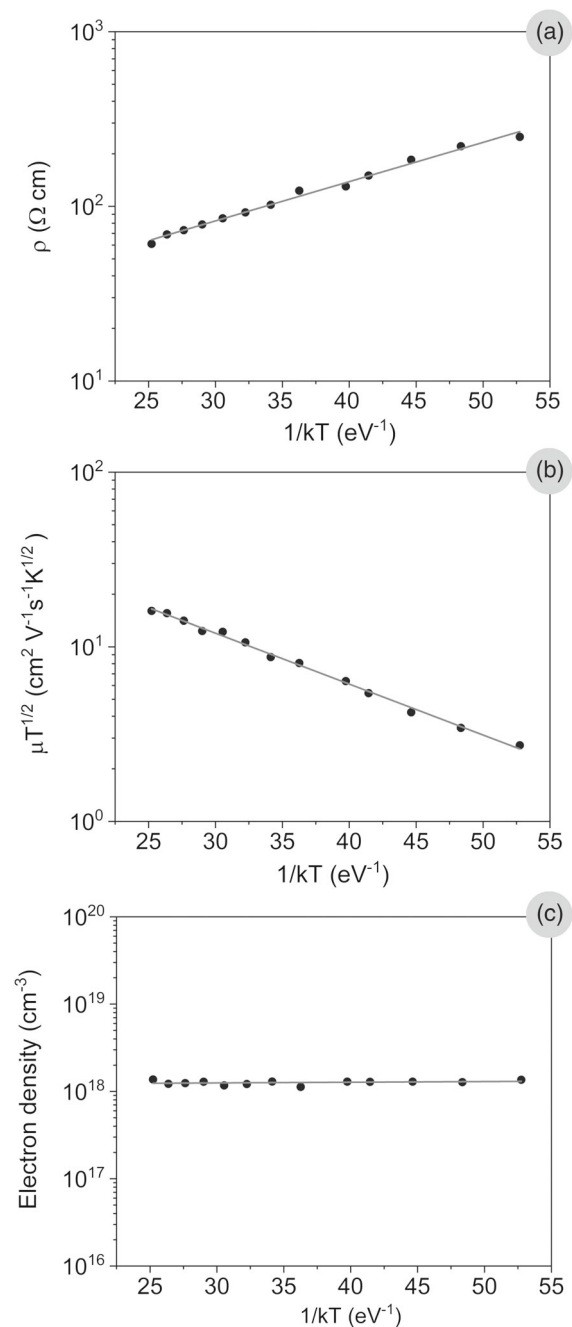


Figure 5. Electrical characterization: Arrhenius plots of a) resistivity, b) mobility, and c) free charge density.

a degenerate semiconductor-like behavior, and we can conclude that the activation energy of free carriers is very close to Fermi level.

The morphological and structural characterizations have shown that the films are made of titania polycrystals in which silver dots are dispersed. The latter do not constitute a continuous network capable of dominating the electric transport process, at least in the investigated temperature range. In contrast, no percolative processes emerge from the measurements carried out in the investigated temperatures range.^[42]

3.3. Raman Spectroscopy

Figure 6 shows that five vibrational peaks at 144, 198, 403, 515, and 638 cm^{-1} are recognizable, and the spectrum is compatible with the characteristic TiO_2 anatase. As largely reported in the literature data, anatase is tetragonal (D_{4h}^{19}) with two formula units per unit cell and six Raman active modes (A_{1g} $2B_{1g}$ $3E_g$ as shown in Figure 6). The peak at 515 cm^{-1} results from overlap of A_{1g} and B_{1g} modes. The peak at 144 cm^{-1} , relative to E_g mode, is a characteristic peak for the bulk anatase phase. A careful analysis of Raman spectra of TiO_2 films has not shown the presence of different phases as tetragonal rutile and orthorhombic brookite. In addition, no signal originated by possible silver–oxygen bonds was detected, such as the band at 490 cm^{-1} , commonly assigned to Ag–O stretching vibration.^[43]

These observations can be consistent with a physical embedding of Ag nanoclusters into a titania dielectric matrix. This is also confirmed by the XRD and SAD analyses.

3.4. UV–Vis Spectroscopy Analysis

Transmittance $T(\lambda)$ and reflectance $R(\lambda)$ spectra of titania–Ag dots films are shown in Figure 7a.

The decrease in transmittivity at low wavelengths indicates the onset of interband absorption (fundamental absorption edge). The refractive index n and extinction coefficient k versus wavelength at normal incidence have been calculated by numerical fit of $R(\lambda)$ and $T(\lambda)$ data as proposed by Heavens and Singer.^[44] Then, knowing T , R , and the thickness t , n , and k can be easily calculated with a numerical fit.^[45]

The optical absorption coefficient $\alpha = 4\pi k/\lambda$ as a function of photon energy $h\nu$ was determined in the fundamental absorption edge region.^[46] The optical bandgap was determined from the analysis of the spectral dependence of the absorption near to the fundamental absorption edge. In this case, the interband absorption theory shows that the absorption coefficient α is given by the following relation

$$F = \alpha h\nu = B(h\nu - E_g)^m \quad (1)$$

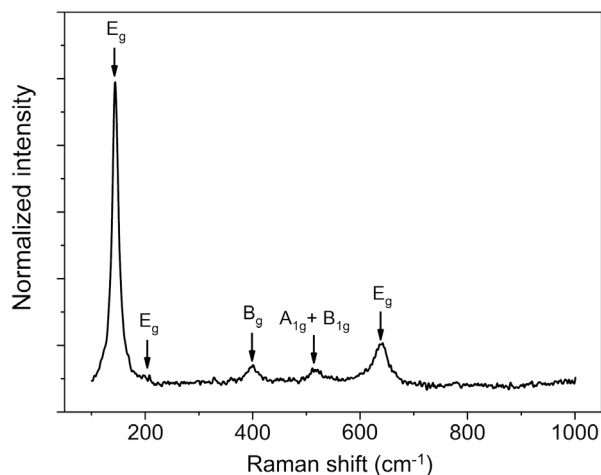


Figure 6. Raman spectrum recorded on a titania–silver dots thin film: the five vibrational peaks typical of TiO_2 anatase are evident.

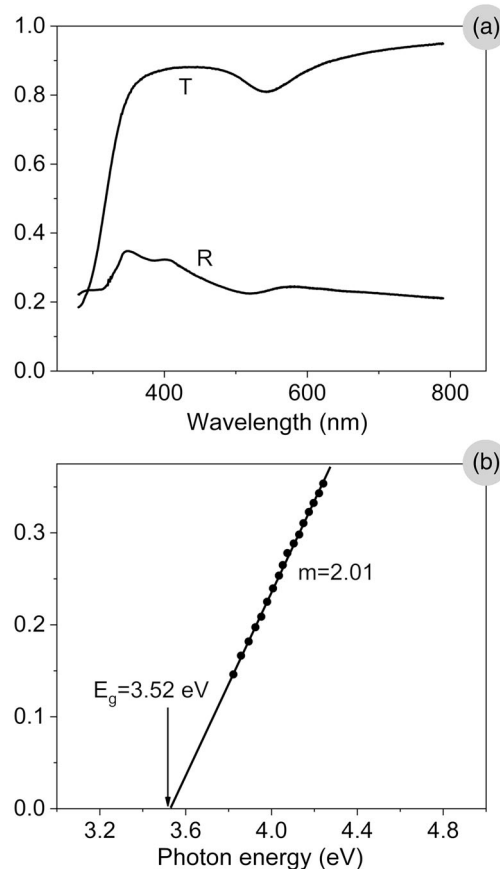


Figure 7. a) Transmittance $T(\lambda)$ and reflectance $R(\lambda)$ spectra of titania–Ag dots films. b) Energy gap determination from the Urbach tail region, Equation (2).

where $h\nu$ is the energy of incident photons and E_g is the value of the optical bandgap corresponding to transitions indicated by the value of m . The factor B depends on the transition probability and can be taken as constant within the optical frequency range. Now, if the first derivative F' of the function F is calculated, with respect to photon energy, then according to Equation (1), the following ratio can be obtained

$$\frac{F}{F'} = \frac{h\nu - E_g}{m} \quad (2)$$

By calculating the value of F and F' from the experimental data, m and E_g can be easily determined from the slope and the intercept with abscissa axis, respectively, of the linear plot of Equation (2) as a function of $h\nu$. This is shown in Figure 7b, where a distinct linear region is evident with the m values of 2.01. This dependence is characteristic of indirect allowed transitions with an energy gap of 3.52 eV. This value is in good agreement with the literature results. It was found that the optical energy gap ranges between 3.1 and 3.7 eV for nano-sized titania.^[47]

Figure 8 shows typical absorbance spectrum acquired on a film: a broad peak at about 530 nm spectral range is clearly visible. It is clearly due to LSPR of silver NPs embedded in

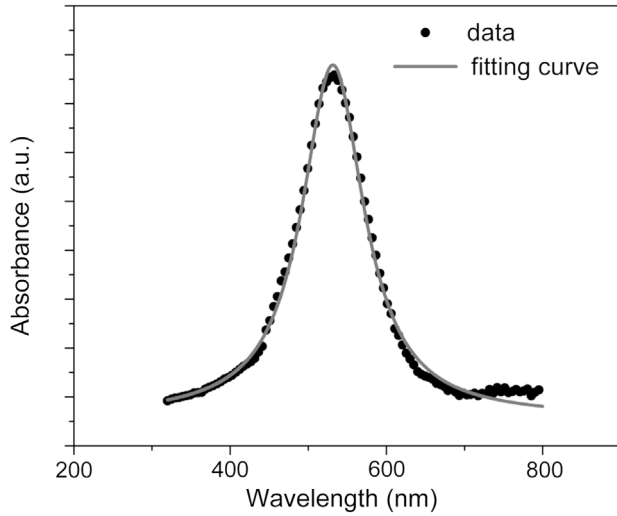


Figure 8. The typical absorbance spectrum acquired on a titania–silver dots thin film (dots) and theoretical fit (solid line).

the titania dielectric film. The plasmon peak is clearly red-shifted with respect to the one already^[48–50] observed from pure silver NP colloidal solutions. Then, absorption spectra have been analyzed according to the light scattering theory proposed by Mie and free electron theory of Drude^[51] to explain the characteristic absorption peak due to surface plasmon resonance.

As evidenced by TEM analysis, the silver dots are dual dispersed, then, according to Mie formalism the absorption coefficient (α_j) due to particles of diameter d_j dispersed in a dielectric medium of permittivity ϵ_m is given by

$$\alpha_j = \frac{18\pi f_j \epsilon_m^{\frac{3}{2}} \epsilon_{2j}}{\lambda(\epsilon_{1j} + 2\epsilon_m)^2 + \epsilon_{2j}^2} \quad (3)$$

where f_j is the volume fraction of the metal particles with diameter d_j , λ is the photon wavelength and $\epsilon_j = \epsilon_{1j} + i\epsilon_{2j}$ is the dielectric function of the particulate material and, extrapolating at optical frequency, the experimental data of Park et al.^[52] and, according to Abdel-Aziz et al.^[53] for nanostructured TiO₂ thin films, in this study, we assume $\epsilon_m = 4.5$.

To consider that there was a finite distribution of particle size, we may write the total absorption coefficient (α) as

$$\alpha = \sum_j \alpha_j \quad (4)$$

The volume fraction of the silver NPs is given by

$$f w_j = f_j \quad (5)$$

where w_j is the weight factor for particles with diameter d_j and is given by

$$w_j = \frac{d_j^3 n_j}{\sum_j d_j^3 n_j} \quad (6)$$

n_j being the number of NPs with diameter d_j . Hence, it can be easily to obtain the size-dependent dielectric function as

$$\epsilon_j(\omega) = \epsilon_{\text{bulk}}(\omega) - \frac{\left(\frac{\omega_p}{\omega}\right)^2}{1 + \left(\frac{2\nu_F}{\omega d_j}\right)^2} + i \frac{2\nu_F \omega_p^2}{\omega^3 d_j} \quad (7)$$

where ω is the photon frequency, ν_F is the Fermi velocity, and ϵ_{bulk} is the permittivity corresponding to interband transitions.

$$\epsilon_{\text{bulk}} = 1 - \frac{\omega_p^2}{(\omega^2 + i\omega\gamma_{\text{free}})} \quad (8)$$

With the damping constant of the electron oscillatory movement^[54] $\gamma_{\text{free}} = 3 \times 10^{13} \text{ s}^{-1}$.

We have fitted the experimental absorption data with d_j and f_j as parameters. In the analysis, we have considered the plasma frequency $\omega_{p0} = 3.7 \times 10^{15} \text{ rad s}^{-1}$ and $\nu_F = 1.38 \times 10^8 \text{ cm s}^{-1}$.^[55]

Figure 8 shows the theoretical fittings (solid gray line) of the representative samples. The reported fit has been obtained for a volume fraction of 93% of NPs having mean size of 40 nm, and a volume fraction of 7% of NPs having mean size of 10 nm.

4. Conclusions

Transparent titania–silver dots thin films were obtained with a simple and economical synthesis method based on the sol–gel technique. The sol–gel formulation has been carefully designed with fluids carefully selected and chosen to avoid the formation of titanium oxide before the solution is deposited by rotation. The formation of the TiO₂ matrix and silver NPs occurs simultaneously during the calcination process at 400 °C.

Only in this way, the silver added in the form of Ag⁺ ions to the sol–gel determines structural and morphological modifications and give rise to films made by a TiO₂ matrix in which the Ag NPs are actually incorporated, as evidenced by the TEM, SEM, and XRD characterizations.

The physical properties of obtained films are strongly affected by the inclusion of Ag NPs into the TiO₂ matrix. In particular, the optical characterization attests that the films have a transmittance higher than 80% and an absorption fundamental edge below 400 nm.

Electrical analysis indicates that the electrical properties of TiO₂–Ag dot films are dominated by the grain boundary scattering and the carrier concentration, in the investigated temperature range, is almost temperature independent. That means, these films show a degenerate semiconductor-like behavior.

The observed plasmonic behavior of TiO₂–Ag dot films undoubtedly represents the most surprising modification of the physical properties of TiO₂. As documented by optical absorption measurements, a strong band was observed at 530 nm. The classical scattering theory of Mie and Drude simulates the absorption spectrum and adapts to the experimental data for a volume fraction of 93% of Ag spherical NPs having an average size of 40 nm and a volume fraction of 7% of Ag spherical NPs having a size of 10 nm.

Supporting Information

Supporting Information is available from the Wiley Online Library or from the author.

Acknowledgements

This work was partially supported by the National Institute of Nuclear Physics (INFN) under the experiment FTM-NEXT.

Conflict of Interest

The authors declare no conflict of interest.

Keywords

nanostructured materials, plasmon resonance, silver dots, thin films, titania

Received: March 4, 2020

Revised: June 3, 2020

Published online: July 14, 2020

-
- [1] K. A. Willets, R. P. Van Duyne, *Annu. Rev. Phys. Chem.* **2007**, *58*, 267.
- [2] S. Mohapatra, Y. K. Mishra, J. Ghatak, D. Kabiraj, D. K. Avasthi, *J. Nanosci. Nanotechnol.* **2008**, *8*, 4285.
- [3] D. K. Avasthi, Y. K. Mishra, R. Singhal, D. Kabiraj, S. Mohapatra, B. Mohanta, N. K. Gohil, N. Singh, *J. Nanosci. Nanotechnol.* **2010**, *10*, 2705.
- [4] A. Buccolieri, A. Serra, G. Giancane, D. Manno, *Beilstein J. Nanotechnol.* **2018**, *9*, 499.
- [5] S. Fu, X. Zhang, Q. Han, S. Liu, X. Han, Y. Liu, *Sci. Rep.* **2016**, *6*, 36701.
- [6] A. Serra, D. Manno, E. Filippo, A. Buccolieri, E. Urso, A. Rizzello, M. Maffia, *Chem* **2011**, *156*, 479.
- [7] E. Filippo, D. Manno, A. Buccolieri, M. Di Giulio, A. Serra, *Superlattices Microstruct.* **2010**, *47*, 66.
- [8] S. Mohapatra, Y. K. Mishra, D. K. Avasthi, D. Kabiraj, J. Ghatak, S. Varma, *J. Phys. D: Appl. Phys.* **2007**, *40*, 7063.
- [9] X. Jiang, S. Hu, Z. Li, J. Lv, G. Si, *Opt. Mater.* **2016**, *58*, 323.
- [10] K. V. Sreekanth, W. Dong, Q. Ouyang, S. Sreejith, M. Elkabbash, C. T. Lim, G. Strangi, K. T. Yong, R. E. Simpson, R. Singh, *ACS Appl. Mater. Interfaces* **2018**, *10*, 34991.
- [11] A. Mahigir, T. W. Chang, A. Behnam, G. L. Liu, M. R. Gartia, G. Veronis, *Sci. Rep.* **2017**, *7*, 14044.
- [12] Z. Zhu, P. G. Evans, R. F. Haglund, J. G. Valentine, *Nano Lett.* **2017**, *17*, 4881.
- [13] K. H. W. Ho, A. Shang, F. Shi, T. W. Lo, P. H. Yeung, Y. S. Yu, X. Zhang, K. Yin Wong, D. Y. Lei, *Adv. Funct. Mater.* **2018**, *28*, 180383.
- [14] E. Almeida, O. Bitton, Y. Prior, *Nat. Commun.* **2016**, *7*, 12533.
- [15] G. A. Niklasson, P. C. Lansåker, S. Y. Li, C. G. Granqvist, *J. Phys. Conf. Ser.* **2016**, *682*, 012003.
- [16] M. L. Brongersma, N. J. Halas, P. Nordlander, *Nat. Nanotechnol.* **2015**, *10*, 25.
- [17] Y. G. Wang, D. C. Cantu, M. S. Lee, J. Li, V. A. Glezakou, R. Rousseau, *J. Am. Chem. Soc.* **2016**, *138*, 10467.
- [18] S. P. Lim, A. Pandikumar, N. M. Huang, H. N. Lim, *Int. J. Hydrogen Energy* **2014**, *39*, 14720.
- [19] J. Li, S. K. Cushing, F. Meng, T. R. Senty, A. D. Bristow, N. Wu, *Nat. Photonics* **2015**, *9*, 601.
- [20] S. Asahi, H. Teranishi, K. Kusaki, T. Kaizu, T. Kita, *Nat. Commun.* **2017**, *8*, 14962.
- [21] S. P. Lim, A. Pandikumar, N. M. Huang, H. N. Lim, G. Gu, T. L. Ma, *RSC Adv.* **2014**, *4*, 48236.
- [22] S. P. Lim, A. Pandikumar, N. M. Huang, H. N. Lim, *RSC Adv.* **2014**, *4*, 38111.
- [23] A. Pandikumar, S.-P. Lim, S. Jayabal, N. M. Huang, H. N. Lim, R. Ramaraj, *Renewable Sustainable Energy Rev.* **2016**, *60*, 408.
- [24] S. Kuriakose, K. Sahu, S. A. Khan, A. Tripathi, D. K. Avasthi, S. Mohapatra, *Opt. Mater.* **2017**, *64*, 47.
- [25] J. Singh, K. Sahu, A. Pandey, M. Kumar, T. Ghosh, B. Satpati, T. Som, S. Varma, D. K. Avasthi, S. Mohapatra, *Appl. Surf. Sci.* **2017**, *411*, 347.
- [26] K. V. Baryshnikova, M. I. Petrov, V. E. Babicheva, P. A. Belov, *Sci. Rep.* **2016**, *6*, 22136.
- [27] K. Nakayama, K. Tanabe, H. A. Atwater, *Appl. Phys. Lett.* **2008**, *93*, 121904.
- [28] C. I. Ho, D. J. Yeh, V. C. Su, C. H. Yang, P. C. Yang, M. Y. Pu, C. H. Kuan, I. C. Cheng, S. C. Lee, *J. Appl. Phys.* **2012**, *112*, 023113.
- [29] J. B. Pendry, *Phys. Rev. Lett.* **2000**, *86*, 3966.
- [30] X. Luo, D. Tsai, M. Gu, M. Hong, *Chem. Soc. Rev.* **2019**, *48*, 2458.
- [31] J. Preclík, P. Galá, F. Trojánek, B. Rezek, Y. Němcová, P. Malý, *J. Appl. Phys.* **2011**, *109*, 083528.
- [32] Y. Liang, S. Sun, T. Deng, H. Ding, W. Chen, Y. Chen, *Materials* **2018**, *11*, 450.
- [33] D. M. Tobaldi, N. Rozman, M. Leoni, M. P. Seabra, A. S. Škapin, R. C. Pullar, J. A. Labrincha, *J. Phys. Chem. C* **2015**, *119*, 23658.
- [34] A. Serra, D. Manno, A. Buccolieri, G. G. Carbone, L. Calcagnile, *Mater. Res. Express* **2019**, *6*, 036206.
- [35] P. Chaudhari, V. Chaudhari, S. Mishra, *Mater. Res.* **2016**, *19*, 446.
- [36] H. A. Dewi, F. Meng, B. Sana, C. Guo, B. Norling, X. Chen, S. Lim, *RSC Adv.* **2014**, *4*, 48815.
- [37] S. Saalimraj, K. C. Ajithprasad, *Mater. Today Proc.* **2017**, *4*, 4372.
- [38] H. Demers, N. Poirier-Demers, A. R. Couture, D. Joly, M. Guilmain, N. De Jonge, D. Drouin, *Scanning* **2011**, *33*, 135.
- [39] C. Gammmer, C. Mangler, C. Rentenberger, H. P. Karthaler, *Scr. Mater.* **2010**, *63*, 312.
- [40] M. Horn, C. F. Schwerdtfeger, E. P. Meagher, *Z. Kristallogr.* **1972**, *136*, 273.
- [41] R. L. Petritz, *Phys. Rev.* **1956**, *104*, 1508.
- [42] A. Serra, D. Manno, T. Siciliano, G. Micocci, A. Tepore, M. Rossi, M. L. Terranova, V. Sessa, S. Piccirillo, S. Orlanducci, *J. Appl. Phys.* **2003**, *94*, 416.
- [43] G. I. N. Waterhouse, G. A. Bowmaker, J. B. Metson, *Phys. Chem. Chem. Phys.* **2001**, *3*, 3838.
- [44] O. S. Heavens, S. F. Singer, *Phys. Today* **1956**, *9*, 24.
- [45] I. Ohlídal, K. Navrátil, E. Schmidt, *Appl. Phys. A* **1982**, *29*, 157.
- [46] R. Rella, A. Serra, G. Micocci, A. Taurino, A. Tepore, D. Manno, *J. Appl. Phys.* **2002**, *82*, 54.
- [47] R. López, R. Gómez, *J. Sol-Gel Sci. Technol.* **2012**, *61*, 1.
- [48] E. Filippo, A. Serra, A. Buccolieri, D. Manno, *Eng. Asp.* **2013**, *417*, 10.
- [49] A. Serra, E. Filippo, A. Buccolieri, M. Di Giulio, D. Manno, *Sens. Actuators, B* **2009**, *140*, 563.
- [50] A. Serra, D. Manno, *Nuovo Cim. Soc. Ital. Fis. C* **2013**, *2013*, 89.
- [51] G. Mie, *Ann. Phys.* **1908**, *25*, 377.
- [52] B. H. Park, L. S. Li, B. J. Gibbons, J. Y. Huang, Q. X. Jia, *Appl. Phys. Lett.* **2001**, *79*, 2797.
- [53] M. M. Abdel-Aziz, I. S. Yahia, L. A. Wahab, M. Fadel, M. A. Affi, *Appl. Surf. Sci.* **2006**, *252*, 8163.
- [54] P. B. Johnson, R. W. Christy, *Phys. Rev. B* **1972**, *6*, 4370.
- [55] D. Manno, E. Filippo, M. Di Giulio, A. Serra, *J. Non-Cryst. Solids* **2008**, *354*, 5515.